# Simultaneous Synthesis and Assembly of Noble Metal Nanoclusters with Variable Micellar Templates

Yao Zhou and Hua Chun Zeng*

NUS Graduate School for Integrative Sciences and Engineering, and Department of Chemical and Biomolecular Engineering, Faculty of Engineering, National University of Singapore, 10 Kent Ridge Crescent, Singapore 119260

Ⓢ Supporting Information

ABSTRACT: Simultaneous synthesis and assembly of Au, Pt, and Pd nanoclusters (NCs; with sizes ≤3 nm) into mesoscale structures with defined boundaries are achieved using their metal halides, cetyltrimethylammonium bromide (CTAB), and thiourea (Tu). Geometric shape, hierarchical organization, and packing density of resultant assemblages vary depending on metal precursors and CTAB concentration. For example, rod- or tube-like assemblages are formed from Au NCs, giant vesicles and/or dandelion-like assemblages from Pt NCs, and rhombic/hexagonal platelet assemblages from PdS NCs and Pd NCs. These assemblages inherit pristine shapes from their respective variable micelles of CTA$^+$−metal halide complexes. Owing to dynamical nature, the assembled NCs demonstrate various structural reforming behaviors. The metal halides, which serve as counterions of positively charged surfactant heads, screen the electrostatic repulsion among the surfactant molecules as well as the micelles, providing the driving force for the formation of soft templates. Meanwhile, the formation of NCs can be addressed from the perspective of nucleation and growth kinetics. The unique protecting role of surface sulfur, controlled release of S$^{2−}$ from Tu, and formation of NCs of metal sulfides as intermediates together lead to a relatively low rate-ratio of growth to nucleation and thus limit the size of product NCs. Our preliminary study also indicates that the assembled noble metal NCs have high catalytic activity and recyclability. In this regard, the present approach not only provides a facile means to construct NC-based metal catalysts but serves also as a simple way to visualize interaction and evolution of micelles of CTA$^+$−metal halide complexes.
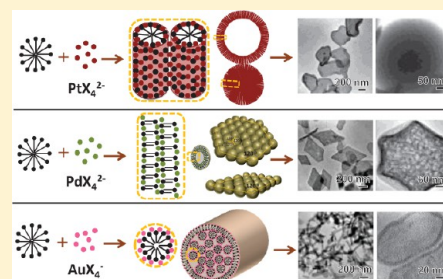
1. INTRODUCTION

Noble metals such as Au,[1] Pt,[2] and Pd[3] and their metal sulfides[4] have found wide applications in many fields: catalysis, bioimaging, sensing, etc.[5] It has been well established that the size of noble metal materials affects their properties and performances significantly.[6] At a size below 3 nm, for example, Au nanoclusters (NCs) lose their bulk-like electronic properties, showing no plasmonic excitation characteristic of relatively large Au nanocrystals.[7] When used as a catalyst, noble metal NCs with a size of 1−3 nm generally have high catalytic activity, good light transparency, and size-dependent properties.[6,8] Because of quantum confinement effects, a luminescence phenomenon is also observed for small-sized noble metal quantum dots (QDs) or NCs.[9,10] To date, a variety of methods are known to prepare noble metal NCs with size below 3 nm. They rely on at least one of the following synthetic techniques: two-phase liquids,[11,12] organic solvents with low polarity,[1,8] strong reducing agents such as NaBH$_4$,[1,11,13] strong protection agents especially alkanethiols,[7,10,13,14] or dendrimer macro-molecules as nanoreactors.[15,16] In addition, large biomolecules have also been employed to produce noble metal QDs below 1 nm.[17] In our search for new possibilities for making noble metal QDs or NCs, in this research, we present a one-phase approach that generates water-soluble Au, Pt, and Pd metal sulfide NCs with a size below 3 nm as reaction intermediates. The major chemicals involved in this synthetic approach are rather simple: cetyltrimethylammonium bromide (CTAB), a widely used cationic surfactant; thiourea (Tu), a commonly used chemical in industry; and metal chloride compounds including HAuCl$_4$, PdCl$_2$, and K$_2$PtCl$_4$ as metal sources. End products Au, Pt, and Pd NCs are formed at a mild reaction temperature below 80 °C, and their particle size could be tuned within a range of 1−3 nm by adjusting process parameters. The formations of sulfide intermediate NCs and final metallic product NCs all can be explained from the standpoints of nucleation and growth kinetics. Our preliminary research also indicates that the as-prepared noble metal NCs have high catalytic activity and recyclability.

In another closely related line, self-assembly of various nano-building blocks with different extents of structural and compositional complexity, such as organic molecules,[18,19] or inorganic nanoparticles (NPs) or their composites,[19−26] into hierarchical organizations has long been investigated.[27] For instance, self-assembly of hydrocarbon amphiphiles has been used widely in various household, research, and industrial applications.[28,29] The assemblages of amphiphilic molecules are dynamic and tunable in both geometry and dimension,[18,30] and

therefore can take on a rich variety of shapes and sizes through micelle interactions.[18,28,31] Giant micelles of surfactants or polymers with well-defined geometric morphologies have been investigated often using cryo-TEM, SAXS, or SANS.[29,32−34] In connection to the above investigations, self-assembly behaviors of hydrocarbon amphiphiles have been applied to nano-technology mainly in two folds. One is to serve as soft templates to direct shaped-controlled synthesis of nanomateri-als.[19,35] In this route, each individual NP is supposed to succeed the shape of the template. The other is as surface modifying agents to change the surface reactivity of preformed NPs and thus to guide the self-assembly of resulting nanocomposites. For instance, giant vesicles of inorganic and organic nano-composites[19−26,36] and ordered mesoporous materials with various architectures[36−38] were formed using different amphiphilic molecules. Such inorganic−organic hybrid frame-works with voids or high porosity are expected to have important applications such as controlled release, nanoreactors, and so on. Nevertheless, in the latter route, macrostructures of such surface-modified NP assemblages are usually independent of giant assemblages of pure surfactants or polymers since these two self-assembly processes often occur in different phys-icochemical environments. In addition, there are also other works in which lipotropic liquid crystals formed from interaction of inorganic metal precursor and micelle solutions were used as soft templates to produce mesoporous metal NPs with hexagonally packed cylindrical mesospace.[39,40] In our present work, the giant micelles of CTA^+−metal halide precursor complexes, in which the metal halide anions are homogeneously distributed as counterions of CTA^+, are formed with various well-defined geometric shapes, and *on-site* sulfidation and/or reduction of confined metal halide precursors by Tu then generate 3D hierarchical assemblages of their corresponding metallic or sulfide NCs. Assemblages of the as-formed NCs well inherit the geometric features of giant micelle precursors. Therefore, for the first time, synthesis of metal NCs and their self-assembly have been integrated in a single micelle-assisted process, and related self-assembly mechanisms of the giant micelle templates have also been addressed at molecular and mesoscopic levels.

2. EXPERIMENTAL SECTION

2.1. Chemicals and Materials. The following chemicals were used as received without further purification: thiourea (Tu, CH_4N_2S, >99%, Alfa Aesar), cetyltrimethylammonium bromide (CTAB, $CH_3(CH_2)_{15}N(Br)(CH_3)_3$, ≥99.6%, Fluka), $HAuCl_4·3H_2O$ (>99.99%, Sigma-Aldrich), K_2PtCl_4 (98%, Sigma-Aldrich), $PdCl_2$ (Sigma-Aldrich), NaOH (Merck, ≥9%), ammonia solution (Merck, 32%), tetraethyl orthosilicate (TEOS, $Si(OC_2H_5)_4$, Sigma-Aldrich, ≥99.0%), 4-nitrophenol (4-NP, $C_6H_5NO_3$, Fluka), sodium borohy-dride (NaBH$_4$, Sigma-Aldrich), polyvinylpyrrolidone (PVP, K30, Fluka), sodium sulfide (Na$_2$S, Alfa Aesar), and hydrazine (N$_2$H$_4$ 30%, Aldrich). Deionized water was collected through the Elga MicroMeg purified water system. Lever-locked plastic syringes (3 mL, National Scientific Co.) and syringe-driven filters (pore size 0.22 μm, JET Biofil) were used to separate catalyst from reaction solution.

2.2. Synthesis, Assembly, and Characterization of Au, Pt, and PdS NCs. As illustrated in Scheme 1, in a typical procedure, without specification, 120 μL of Tu (0.25 M) and 10 μL of NaOH (15.0 M) were mixed with 10.0 mL of deionized water and stored in an electric oven at 80 °C (named as solution A). At the same time, 1.0 mL of an aqueous solution of noble metal precursors, namely HAuCl$_4$ (0.01 M), PdCl$_2$ (0.01 M, pH = 1.0), or K$_2$PtCl$_4$ (0.01 M), and 100 μL of CTAB solution (0.10 M) were mixed in 10.0 mL of deionized water (denoted as solution B) and stirred at room temperature. After 0.5 h,

Scheme 1. Main Experimental Conditions and Operations for Preparation of NCs and Their Assemblages
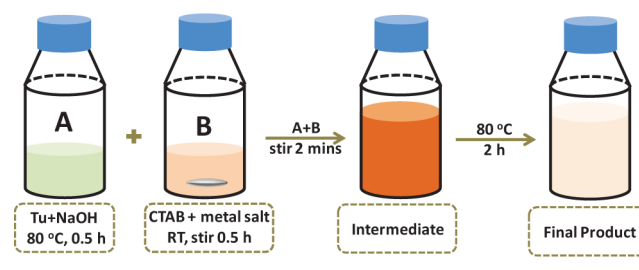
solution B was added into solution A. After stirred for 2 min at ambient conditions, the solution mixture was either kept static in the electric oven or stirred in an oil bath at 80 °C for 1−2 h to generate final products. Note that the volume of metal precursors used in each case was fixed at 1.0 mL; any changes in concentration of CTAB, molar ratio of CTAB to metal precursor (r_c), concentration of Tu, pH value, and reaction temperature would be specified when necessary.

Apart from the above final products, solid intermediates (i.e., noble metal sulfide NCs) were also prepared. In doing so, within 1 min after mixing solution A and solution B, the mixture was immediately centrifuged at 6000 rpm for 10 min, and this step was repeated twice by replenishing with 5.0 mL of deionized water to get intermediate precipitate for analysis.

The as-prepared colloidal suspensions were characterized by transmission electron microscopy (TEM, JEM-2010, 200 kV) and high-resolution TEM (HRTEM, JEM-2100F, 200 kV). X-ray photo-electron spectroscopy (XPS, AXIS-HSi, Kratos Analytical) analysis was conducted using a monochromatized Al Kα exciting radiation ($h\nu$ = 1286.71 eV) with a constant analyzer-pass-energy of 40.0 eV. All binding energies (BEs) were referenced to C 1s peak (BE set at 284.5 eV) arising from C−C bonds. Besides, the colloids in the Au case were characterized by UV−vis spectrometry (UV-2450, Shimadzu) and laser light scattering (LLS) analysis using a particle size analyzer (Brookhaven 90Plus). The as-obtained PdS NC assemblages, after being washed with deionized water twice, were subjected to TGA analysis in nitrogen atmosphere (DTG-60AH, Shimadzu) with a gas flow rate of 50 mL/min and heating rate of 10 °C/min. Metallic Pd samples prepared by reducing the PdS NC assemblages with NaBH$_4$ was also analyzed by TGA under the same conditions.

2.3. Silica Coating of the Assemblages. In a typical process, 3.0 mL of the as-prepared colloid solution was centrifuged at 6000 rpm for 10 min and re-dispersed in 3.0 mL of deionized water, followed by addition of 0−160 μL of 0.10 M CTAB solution. Then 10 μL of TEOS ethanol solution (volume ratio of TEOS to ethanol was at 1:1) was added and stirred for 2 min. Afterward, 10 μL of concentrated ammonia solution was added. After stirred vigorously for 12 h, the mixture solution was centrifuged at 6000 rpm for 10 min, and the precipitate was re-dispersed in ethanol, which was then centrifuged at 4000 rpm for 10 min. The precipitate obtained was termed as silica-coated assemblages in subsection 3.4.

2.4. Preliminary Investigation of Catalytic Performance of NCs. As an example to show the high catalytic activity of the as-prepared NCs assemblages, the assemblages from the Pd case were used as catalyst for reduction of 4-NP by NaBH$_4$. In a typical process, 8.0 mL of 2.31 mM 4-NP aqueous solution was added into 50.0 mL of deionized water, followed by addition of 10.0 mL of freshly prepared 0.325 M NaBH$_4$ aqueous solution; afterward, into the mixture, 5.0 mL of as-prepared PdS NCs colloid, after being washed and redispersed in 5.0 mL of deionized water, was added and magnetically stirred. To monitor the progress of the reaction, every 3 mL of the reaction solution was withdrawn using a syringe, which was then passed through a filter with pore size of 0.22 μm and then subjected to UV−vis spectroscopic analysis. The reaction was carried out at room temperature (23 °C).

To test the catalytic stability of the Pd NCs assemblages, 1.0 mL of 2.31 mM 4-NP aqueous solution was mixed with 10.0 mL of freshly

prepared 0.325 M $NaBH_4$ solution, followed by addition of 5.0 mL of as-prepared colloidal PdS NCs. When the deep yellow color of the reaction solution fade away, the mixture was centrifuged at 12 000 rpm for 5 min; then the black catalyst precipitate was redispersed in the mixture of 5.0 mL of deionized water and 100 μL of 0.10 M CTAB. Afterward, the above reduction reaction was repeated using thus-recycled catalyst. The same catalyst was recycled for eight times. The time starting from the addition of catalyst to the disappearance of the yellow color of the solution was recorded as the minimum time of reaction (t_m).

3. RESULTS AND DISCUSSION

3.1. Formation and Assembly of Au NCs. As depicted in Scheme 1, addition of solution B into solution A was accompanied by immediate color changes. The resultant Au NCs actually arranged themselves into different nano- or mesoscale assemblages depending on CTAB concentration, as shown in Figure 1. With a high molar ratio of CTAB to $HAuCl_4$, e.g., r_c = 10:1, the shape of assemblage is not very well defined. Quasi-spherical aggregates and freestanding NCs are both present (Figure 1a). Reducing the molar ratio of CTAB to $HAuCl_4$ to 1:1, the product has a well-defined rod-shape with a length varying from several tens to a few hundred nanometers (Figure 1b). These one-dimensionally assembled Au NCs are fairly stable under an electron beam. Our LLS analysis also reveals that the average equivalent hydrodynamic diameter of the assembled Au NCs is around 154 nm (Figure S1). Different from single-crystalline Au nanorods,[41] the "nanorods" reported herein consist of numerous NCs with a size below 3 nm (Figure 1c,d). Consistent with the TEM result, average hydrodynamic diameter of Au NCs is around 3.6 nm (Figure S1). Most of the NCs exist discretely, though oriented attachment among them might be observed occasionally. The size of the NCs could also be adjusted by changing Tu concentration. For example, an average size of NCs was 3.2 nm using 40 μL of Tu (Figure 1c), whereas it decreased to 2.8 nm with 200 μL of this chemical (Figure 1d). Our HRTEM analysis gives two interplanar distances, 0.21 and 0.24 nm, which are assigned to d_{111} and d_{200} of Au respectively (Figure 1e and Figure S2). XPS spectrum (Figure 1f) of this sample exhibits a major BE peak of Au $4f_{7/2}$ at 83.6 eV which corresponds to typical metallic Au^0 species.[42] The combined investigation of HRTEM/XPS thus confirms the formation of metallic Au NCs. In addition, optical properties of Au NCs with a size below 3 nm are distinctly different from their larger counterparts.[12,14,43] In contrast to colorful colloidal suspension of larger Au nanocrystals, the color of our Au NC solution is milky opalescent; no characteristic SPR absorption band can be found in the range of 500 to 800 nm of its UV−vis spectrum in Figure 1g. And as shown in Figure 1h, excitation of the Au NC colloid at 258 nm generates two emission bands, a strong one at 328 nm and a weak one at 628 nm, demonstrating the quantum confinement effect of those NCs.

Moreover, in Figure 2a,b, the TEM image contrast along the edge of each as-prepared "rod" is almost identical to or even lighter than the central area. It indicates that, in solution phase, these "rods" did not hold an interior cavity; otherwise the edges of a tubular structure would have had a darker image contrast than the central area. We found that such structures are only metastable, and their shape is evolvable with post treatment. In Figure 2c,d, for example, addition of CTAB into the as-prepared Au NC assemblages leads to decrease in aspect ratio of these "particulate rods". More importantly, the image contrast of the assemblage edges increased gradually with
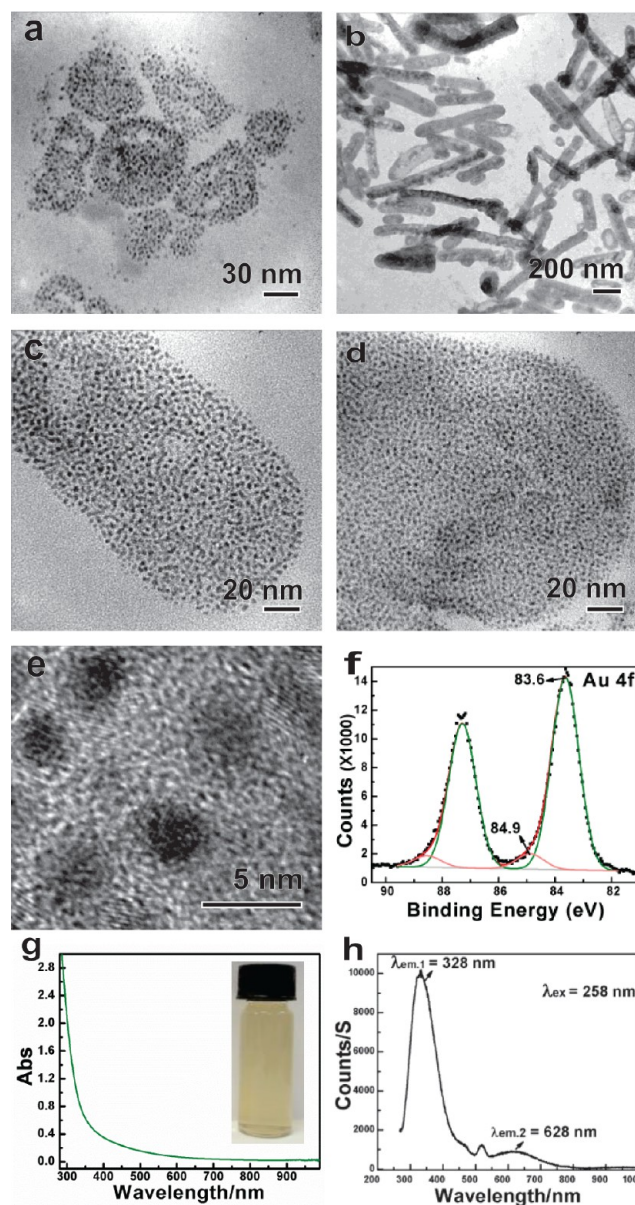
Figure 1. TEM images of (a) Au NC assemblages prepared with a molar ratio of CTAB to $HAuCl_4$ (r_c) at 10:1, (b,c) nanorod-shaped Au NC assemblages prepared with the r_c at 1:1 using 40 μL of Tu, and and (d) 200 μL of Tu, and (e) HRTEM image of as-prepared Au NCs. (f) Au 4f XPS spectrum of as-prepared Au NCs; the black dots are the experimental data, the green and pink lines are the deconvoluted peaks, and the red line is the sum of the fitted data, similarly for the XPS data hereinafter. (g) UV−vis spectrum and photograph (inset) of the colloidal suspension of Au NCs, and (h) emission spectrum of the colloidal suspension of Au NCs excited at 258 nm.

increasing CTAB in the post treatment (Figure S3), indicating a structural transformation from "solid rods" to enclosed hollow vesicle assemblages of Au NCs. Based on this TEM result, Figure 2e illustrates that the Au NCs in the hollow assemblages are located in the wall region. Such vesicles are flexible yet integral. They could adjust themselves into a monolayer array upon drying (Figure 2c). The wall thickness of hollow vesicle assemblages could be determined from their "edges", which is around 12 nm (Figure 2d).

As illustrated in Figure 2e, the "nanorods" are filled with randomly distributed Au NCs which would interact with each
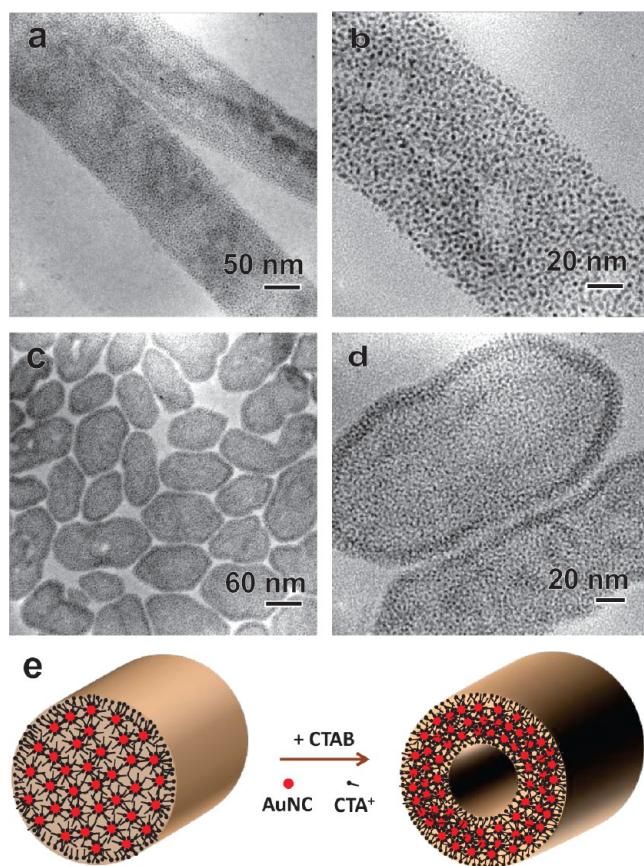
Figure 2. TEM images of (a,b) the as-prepared nanorod-like assemblages of Au NCs and (c,d) formation of enclosed hollow vesicles of Au NCs after addition of 200 μL of 0.1 M CTAB into 3.0 mL of the as-prepared colloid of Au NCs. (e) Schematic diagram of structural transformation of nanorod-like assemblages of Au NCs to enclosed hollow vesicles of Au NCs with addition of CTAB. The cross-sectional views depict the arrangements of Au NCs and surfactant molecules inside the assemblages. Note that the depicted objects in (e) are not proportional to real dimensions (similarly for other schematic diagrams hereinafter).

other through van der Waals attractive force arising from their entangled hydrocarbon chains of CTA$^+$ whose head groups attach to the Au NCs. Since the shape of the "nanorods" is well defined, it is expected that the Au NCs are confined within a large micelle with CTA$^+$ head groups pointing to the water phase and that the hydrophobic tails interact with the hydrocarbon chains of CTA$^+$ on Au NCs (Figure 2e). Thus, the content within the micelles is considered as an "oil" phase. Further addition of CTAB improved dispersion of "oil" phase in water, since surfactants in general promote the dispersion of one phase in another immiscible phase by adsorbing at their interface and decreasing surface tension. Meanwhile, the newly added CTAB would disturb the various force balances initially established within the "oil" phase as well as at the "oil"−water interface. The observed restructure and expansion in the hollow assemblages are a natural response to reestablish new balances among different forces. Manipulation of such dynamic Au NC assemblages as artificial micelles through other post treatments to further craft the Au-based nanostructures is also possible.

The formation and assembly of Au NCs are also determined sensitively by the pH value of solution. On the one hand, when no NaOH was added to solution A, chain-like networks comprised of Au NCs at a size around 5 nm were obtained

(Figure S4). On the other hand, addition of inorganic acids such as HNO$_3$ into the as-formed colloidal Au NCs would lead to NC aggregation and formation of much larger Au nanocrystals within the above hollow assemblages (Figure S4).

3.2. Formation and Assembly of Pt NCs. For the case of precursor salt K$_2$PtCl$_4$, both stirred and unstirred reaction environments cause a significant difference in Pt NC assemblages in addition to the molar ratio of CTAB to the metal precursor. In Figure 3a,b, irregular vesicles with well-
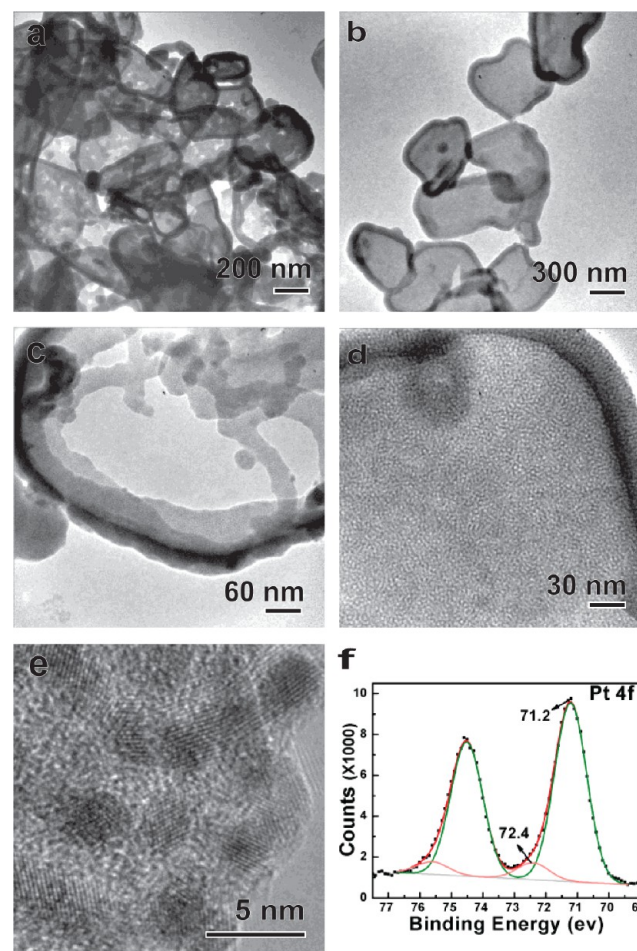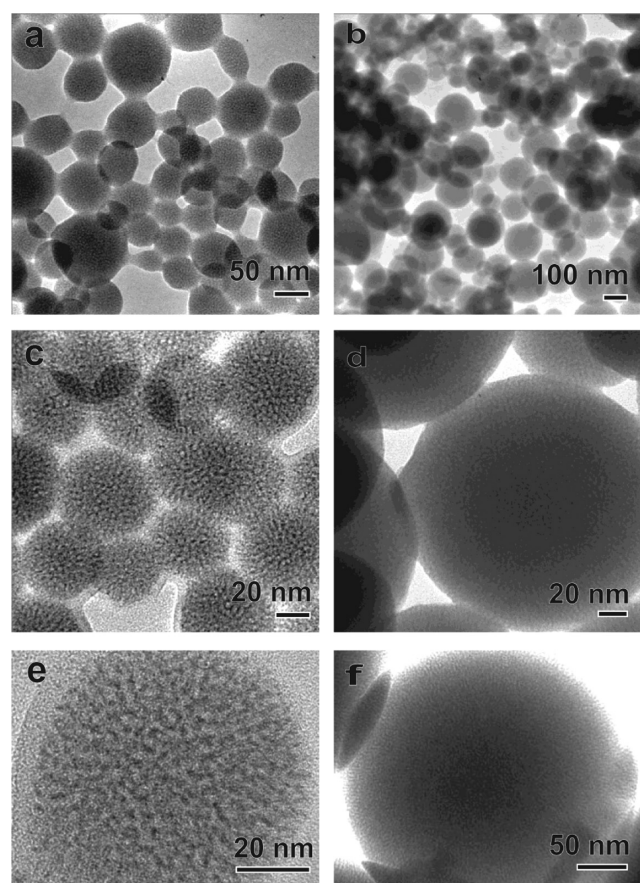

Figure 3. TEM images of dried giant vesicles formed from self-assembly of Pt NCs synthesized (r_c = 1:1) at (a,c) 80 and (b,d) 60 °C, (c) a ruptured vesicle with overlapping of two layers around the boundary, and (d) the porous continuous wall of an intact vesicle structures, and (e) HRTEM image of the Pt NCs in the wall region of vesicle. (f) the Pt 4f XPS spectrum of the giant vesicles of Pt NCs.

defined boundaries were formed when the mixture of solutions A and B was kept still inside the oven and a relatively large amount of CTAB was used (e.g., the molar ratio of CTAB to K$_2$PtCl$_4$ larger than 1:1). Such vesicles are pretty large in size, and their spatial dimension can be more than 1000 nm. At 60 °C, a longer reaction time is required in order to complete the reaction (Figure 3b,d). At 80 °C, the reaction time can be shortened, but product vesicles are found to rupture into irregular fragments easily, as shown in Figure 3a,c and Figure S5. In general, low reaction temperature and high CTAB concentration produce stable vesicles of this type. Figure 3b,d demonstrates that high structural integrity can be maintained when these vesicles reside on a TEM sample grid. Wall

overlapping at the vicinity of boundary can also be identified (Figure 3c). It verifies that the structures observed were hollow vesicles in solution. The wall thickness of the vesicles was registered in the boundaries (Figure 3a−d and see Figure 5e later), which are around 30−35 nm. At a relatively high magnification, one can observe that the Pt NCs (their size at 2.6 nm) actually arranged themselves into lines (Figure S5), giving rise to inter-particulate spaces perpendicular to the surfaces of vesicles (Figure 3d,e, Figure S6, and Figure 5e). Nevertheless, most of Pt NCs are still present discretely, though oriented attachment did occur occasionally among neighboring NCs (Figure 3e and Figure S6). The hollow assemblages of Pt NCs could be considered bicontinuous in both water phase and "oil" phase.[19] Our HRTEM study reveals that typical lattice fringe of NCs is 0.23 nm (i.e., d_{111} of Pt). Consistent with this, our XPS analysis gives a major BE peak of Pt $4f_{7/2}$ at 71.2 eV, which belongs to the metallic Pt^0 (Figure 3f).[44]

Instead of forming hollow structures, in Figure 4a,c,e, porous dandelion-like assemblages of Pt NCs with diameter below 80

assemblages are also porous in nature. The inter-particulate spaces are resulted along the surface normal, similar to those in the walls of vesicles in Figure 3 (Figure 5e).

Figures 3 and 4 together indicate strong assembling dependency on the reaction conditions and low stability of the giant vesicles. When 100 μL of CTAB (r_c = 1:1) was used and the mixture solution was kept unstirred in an oven of 80 °C for a period of 18 h, reported in Figure 5a, the dandelion-like
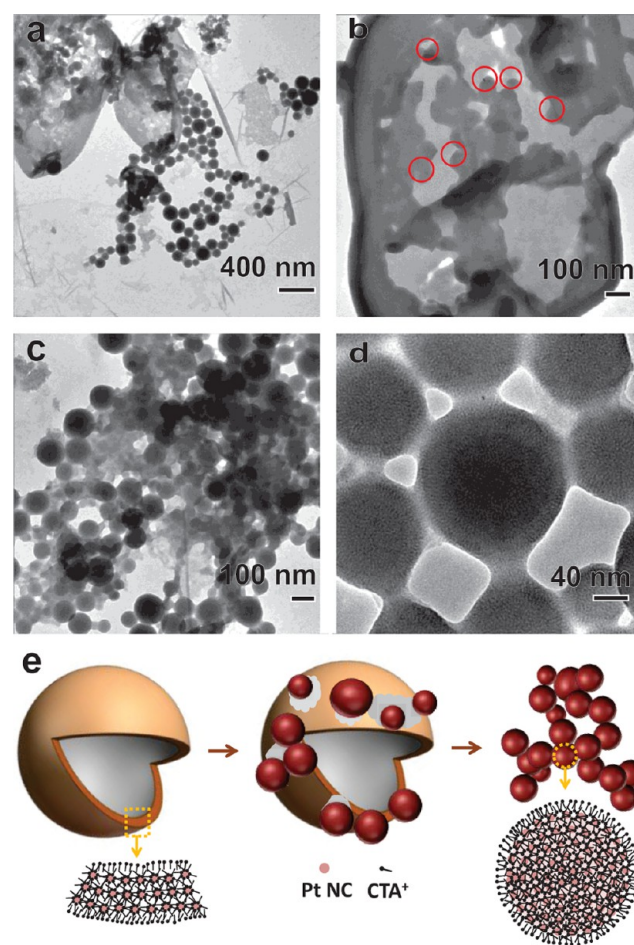

Figure 5. Evolution of dandelion-like Pt NC assemblages from a giant vesicle through a budding process (TEM images): (a) coexistence of vesicles with "dandelions", (b) a vesicle which starts to rupture and generate "dandelions" (where red circles indicate forming intra-membrane domains/buds), (c) a disappearing parental vesicle from which many "dandelions" were produced, and (d) the as-formed "dandelions" interconnected with each other through a neck. (e) Schematic diagram of the above budding process. The bottom illustrations correspond to cross-sectional views of the shell of hollow vesicle and the compact dandelion-like assemblage.

Figure 4. TEM and HRTEM images of dandelion-like assemblages of Pt NCs synthesized with different amounts of CTAB: (a,c,e) 100 μL, with r_c at 1:1, and (b,d,f) 50 μL, with r_c at 0.5:1. Note that the reaction solution was stirred throughout the course of synthesis in (a,c,e), and the reaction temperature was set at 80 °C.

nm and some threadlike aggregates of Pt NCs (Figure S7) were generated under the same reaction conditions of Figure 3 but with additional stirring throughout the whole reaction process. When the CTAB content was decreased (e.g., to 50 μL), much larger spherical assemblages of Pt NCs were formed (Figure 4b,d,f). As shown in Figure 4d,f and Figure S7, the spherical

assemblages and erupted giant vesicles of Pt NCs coexist in the same sample. The "dandelions" were actually formed from the parental giant vesicles, as described in Figure 5e. Figure 5c clearly shows the end stage of such a structural reform where small "dandelions" are born from disappearing parental vesicles. Interestingly, this process is analogical to the ubiquitous budding process in biomembrane in many aspects.[45,46] First, the requisite for a budding process to take place is that the membrane matrix should be in a fluid state.[45] In our present case, the walls of giant vesicles are composed of numerous NCs, which are dynamical in nature and fulfill this requirement.

Second, formation and growth of a so-called intramembrane domain is necessary to initialize a budding process.[47] During the growth, the edge energy of a domain is proportional to its length. Therefore, the domains tend to attain a circular shape to achieve minimum edge energy.[47] The NCs within the membrane may undergo coalescence due to van der Waals attractive force. In Figure 5b, though they are not particularly well defined, circular morphology can also be identified; presumably they are the "forming buds". Third, the resulting buds are normally connected with their parental vesicles with a thin neck.[45,46] In Figure 5c,d, the as-produced spherical aggregates are indeed connected with each other by such "necks". The stirring added in synthesis could initialize this budding process by rupturing the vesicles and help the maturing buds to pinch off (Figure 4a,c,e). However, formation of intramembrane domains is disfavored at a higher CTAB content due to higher electrostatic repulsive forces among NCs or at a lower temperature due to slower diffusion rate of NCs, which can explain why the giant vesicles (Figure 3b) are relatively stable at higher CTAB concentration or at lower reaction temperature.

3.3. Formation and Assembly of PdS/Pd NCs. When PdCl$_2$ was used as a precursor salt at a relatively low CTAB concentration, rhombic and hexagonal "platelets" were produced as displayed in Figure 6a,b. The boundaries of the platelets are well defined; their edges have an adjacent angle of either 60° or 120°. The rhombic and hexagonal platelets are porous and consist of numerous NCs (Figure 6c,d). The NCs seem to assemble themselves in a disordered manner. Similar to the Au case, the dosage of Tu in synthesis dictates the size of NCs. The average sizes of NCs were 2.8 nm (Figure 6c) and 3.4 nm (Figure 6d) when 120 and 40 μL of Tu were used, respectively. In addition, there are some platelets with shapes resembling rectangles in the sample (Figure S8). Different from those in rhombic and hexagonal platelets, the NCs in the rectangular platelets are highly ordered along the longitudinal axis (Figure S8). Moreover, shown in Figure 6a−d, the surfaces of platelet are rough; the local contrast varies notably indicating variation in distribution of NCs. Our XPS analysis reveals a major BE peak of Pd $3d_{5/2}$ at 336.3 eV (Figure 6f), slightly higher than the typical BE of Pd^0 $3d_{5/2}$ which is at the range of 335.0−336.0 eV but much lower than the typical BE of Pd^{2+} that should be at around 337.5 eV.[48] The peak is thus assigned to Pd^{2+} of PdS,[49] rather than Pd^0. Consistent with the XPS result, two lattice fringes, i.e., 0.23 and 0.22 nm, are assigned to interplanar distances d_{220} and d_{212} of PdS (HRTEM image, Figure 6e). Interestingly, these PdS NCs can be converted to metallic Pd NCs by reducing agents (e.g., N$_2$H$_4$), and the original shapes of the platelets can still be preserved, as shown in Figure 6g,h.

Attempt to explain the formation mechanism of such polygonal platelets is challenging. However, we note that porous liquid crystals of hydrocarbon amphiphiles with well-defined shapes such as cubosomes and even hexasomes have been reported.[50,51] Macrostructures of these liquid crystals are homogeneous and have highly ordered channels which are believed to be formed from cubic or hexagonal packing of the amphiphilic molecules,[50,51] which are quite different from our hexagonal or rhombic platelets. In Figure 6 and Figure 7, the hexagonal or rhombic platelets are likely formed from coalescence or fusion of smaller vesicles, as depicted in Figure 7e. First, at a high CTAB concentration, we found that either vesicles or hexagonal assemblages were produced depending on
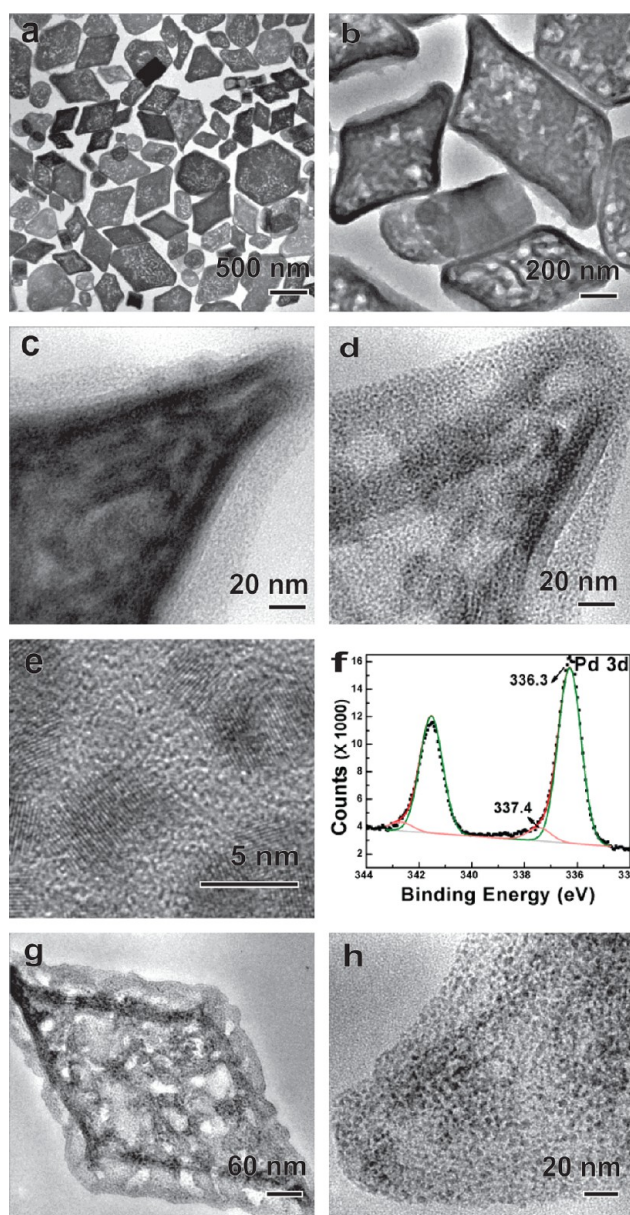
Figure 6. TEM images of PdS NC platelets synthesized using 100 μL of CTAB (r_c = 1:1) and (a,b,c) 120 μL and (d) 40 μL of Tu, respectively. (e) HRTEM image of the PdS NCs in (d). (f) Pd $3d$ XPS spectrum of PdS NCs. (g,h) TEM images of rhombic Pd NC assembalges formed from reducing 2.0 mL of the as-formed colloidal suspension of PdS NCs with 100 μL of 33.0% N$_2$H$_4$.

whether the reaction solution was stirred or not. Specifically, when the reaction mixture was stirred and 200 μL of CTAB was used, round vesicles with diameters ranging within 50 and 200 nm were observed, as shown in Figure 7a. These vesicles are also composed of NCs, which occasionally are arranged in an ordered or semi-ordered manner (Figure 7e). Different from the giant vesicles observed in the Pt case, the vesicles observed here are much smaller in size and have much thinner walls, and almost all of them are ruptured. Surprisingly, when the same reaction mixture was kept unstirring over the course of synthesis, hexagonal platelets were the main product morphology (Figure 7b). The side length of the hexagonal platelet varies from 200 to 500 nm. Similar to the rhombic platelets, the hexagonal platelets also have rough surface and uneven local
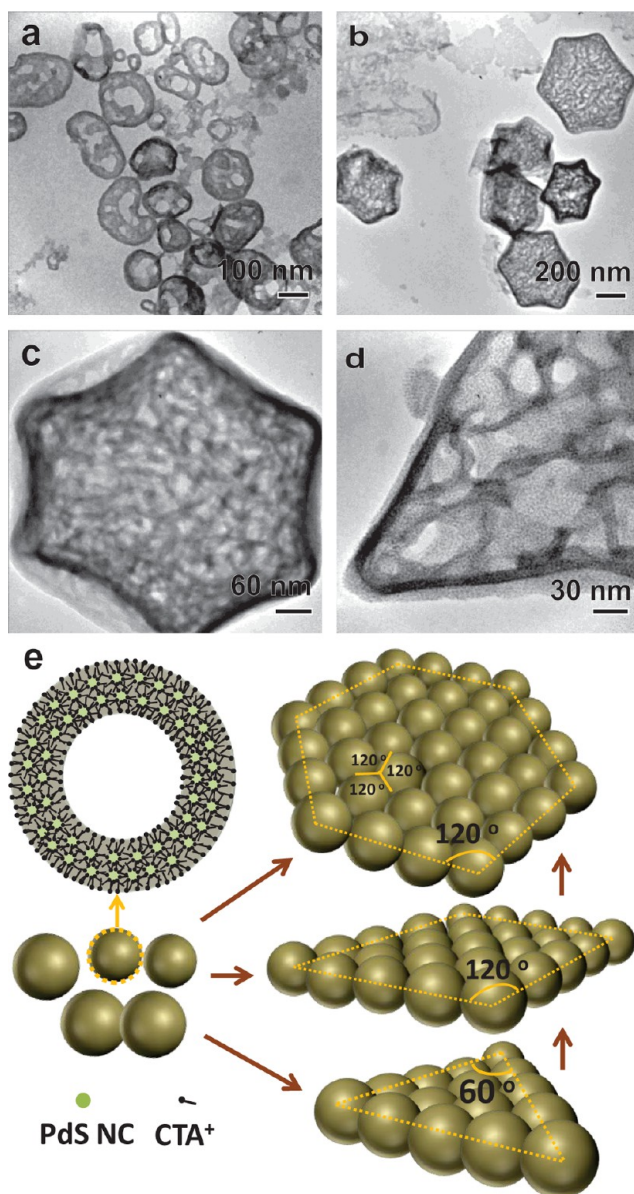
Figure 7. TEM images of (a) ruptured PdS NC vesicles formed with a stirred reaction, (b,c) hexagonal platelet-like PdS NC assemblages formed without stirring [note that 200 μL of CTAB (r_c = 2:1) was used in the syntheses shown in (a,b,c)], and (d) a perforated rhombic platelet-like PdS NC assemblage with compartmented vacant spaces formed upon drying. (e) Schematic diagram of coalescence of individual vesicles into triangular, rhombic and hexagonal platelets. The illustration in the upper left in (e) is a cross-sectional view of the vesicle.

contrast in their body phase (Figure 7c). It seems that at this CTAB concentration (e.g., 200 μL, r_c = 2:1), magnetic stirring ruptured the vesicles and prevented them from coalescing or fusing into a hexagonal platelet. When the CTAB concentration was low (e.g., 100 μL), the vesicles would be more compact and the repulsive electrostatic force among vesicles was lower, so they could still manage to coalesce, even though the reaction solution was stirred. Second, this explanation is validated by the fact that the as-formed platelets have unevenly distributed NCs, because the areas where the vesicles merged would have higher populations of NCs than their interior voids. In Figure 7c,d, these rhombic/hexagonal platelets show plenty vacant spaces,

which likely correspond to merging cavities from vesicle units upon drying.

The balance between van der Waals attractive force and repulsive electrostatic force plays an important role in regulating the coalescence of vesicles. In principle, identical to emergence in soap bubbles (which represent another type of vesicles),[52] the surface area minimization is a thermodynamic driving force for the coalescence or fusion of several small vesicles into a larger one. Moreover, as shown in Figure 7e, the rhombic or hexagonal platelets produced are observed with two adjacent angles of 120° and 60°. According to the classical Plateau's law,[52,53] which has also been mathematically verified, when three bubbles of similar size coalesce, the coplanar angles at which they incline are always equal to each other, which is exactly 120° (Figure 7e); coalescence through any other ways is unstable and will undergo structural reforming. Naturally, such a requirement on the assembly geometry of spherical building blocks would lead to formation of hexagonally packed vesicles. Besides, formation of hexagonal shape is also thermodynamically favorable. A hexagon is known to enclose maximum space with minimum perimeter; it is efficient in minimizing the surface energy of a system. During the soap bubble coalescence process, the bubble film will shrink, and air trapped inside the bubble will find way to expand.[52] Each vesicles located inside the body phase of the platelet will interact with its neighboring vesicles through infusion of walls, leading to changes in size and shape of voids as well as variation in wall curvature.

Simple calculation also reveals that the specific surface area of polygonal platelets, given identical thickness and volumes, decreases with increasing numbers of edges, and the strain tension at the three vertices of an equilateral triangle platelet is relatively high. This perhaps could explain why triangular platelets were only observed occasionally in our syntheses. In Figure 6a, furthermore, the hexagonal platelets are generally larger than the rhombic ones. In this regard, growth or combination of triangular platelets to rhombic platelets and finally to hexagonal platelets is thermodynamically favorable, which indeed governs the structural evolution of assemblages of PdS NCs and Pd NCs (Figure S9 and the illustration of Figure 7e).

From the above results, we can see that the morphology of a mesoscale assemblage depends on the nature of metal salts and CTAB concentration employed in synthesis. In general, at the constant concentration of a metal precursor, increase in CTAB concentration leads to decrease in overall density of assemblages. For example, solid porous spherical "dandelions" were formed with CTAB = 50 μL (Figure 4b), whereas giant vesicles were formed with CTAB = 100 μL (Figure 3a) in the case of Pt (see Scheme 2d later). Similar trend was also observed in the cases of Au (Scheme 2b) and Pd (Scheme 2c). Regarding different metal precursors, the gap among neighboring NCs in the Au NC assemblages (Figure 1e) is much larger than that in the cases of Pt (Figure 3e) and PdS (Figure 6e) under the same magnification of TEM image. That is, the local NC number density of assemblages in the Au case is much lower than those in the cases of Pt and Pd, which will be explained later.
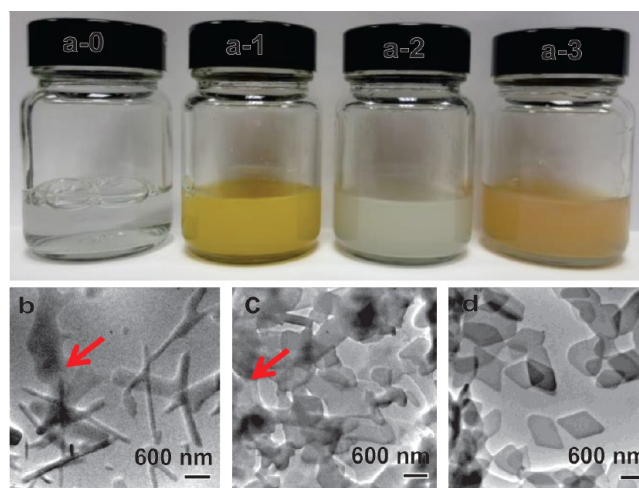
3.4. Capture of the As-Formed Assemblages. To further confirm that the above NC assemblages were formed in the solution rather than on the TEM copper grid, typical assemblages from the cases of Au and Pd were coated with silica. As exemplified in Figure 8, a thin layer (with a lighter contrast) of silica was observed at the boundary of each
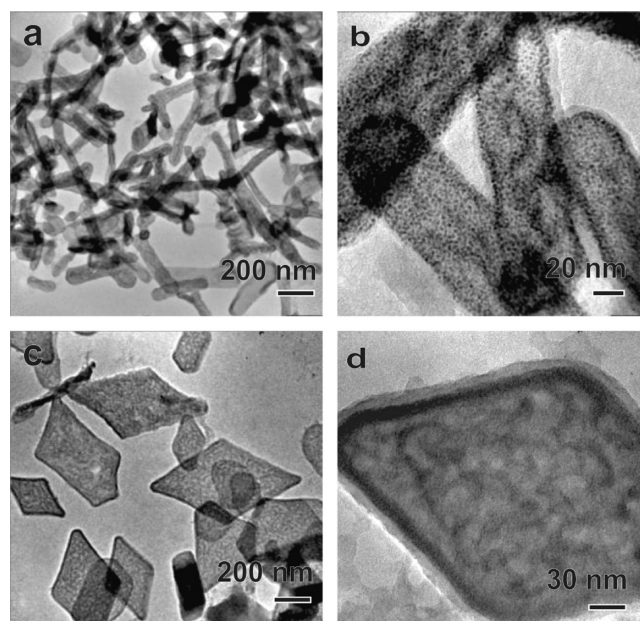
Figure 8. TEM images of (a,b) silica-coated Au NC assemblages and (c,d) silica-coated rhombic PdS NC assemblages.

Figure 9. Photograph and TEM images of transparent solution of CTAB surfactant (a-0), colloidal suspension of CTAB and HAuCl$_4$ (a-1,b), colloidal suspension of CTAB and K$_2$PtCl$_4$ (a-2,c), and colloidal suspension of CTAB and PdCl$_2$ (a-3,d) with r_c at 1:1. The red arrows indicate fast deshaping of metal precursor–CTAB complexes under the exposure of an electron beam.

nanorod or rhombic platelet, indicating *in situ* silica formation and thus successful capture of the assembled structures. The thickness of silica coating could be adjusted with concentration of TEOS. The morphologies of the overall assemblages and individual NCs were well preserved in this coating process. After silica coating, the NC assemblages could be well redispersed and exist stably in ethanol solvent. These results directly prove that the assemblages reported in the previous subsections were indeed preformed in the bulk solution rather than on the copper grid substrate during our TEM sample preparation (i.e., drying processes).

3.5. Counterion-Induced Self-Assembly of Micelles with Templated-Assembly of NCs. The CTAB solution itself is a colorless transparent liquid as shown in the photograph (a-0) of Figure 9. Upon the addition of transparent metal ion–chloride complexes aqueous solutions, their mixture would turn highly turbid gradually (a-1, a-2, and a-3). The three mixtures were sampled directly for TEM examination to understand the interaction of CTAB with these noble metal precursors. As expected, the metal precursor-CTAB complexes are not stable under an electron beam. Quite surprisingly, however, they give similar geometric shapes as their corresponding end products. In Figure 9b, well-defined nanorod-shaped structures were observed in the case of Au, though they were deshaped rapidly under an electron beam as marked by the red arrows. Two-dimensional lamellar structures with well-defined boundaries, which are quite similar to the giant vesicles (Figure 3a–d), were observed in the case of Pt, and they shrunk severely under the electron beam (Figure 9c). As for the case of Pd, triangular, rhombic, and hexagonal platelets were also observed (Figure 9d). Considering the close similarity in the geometric shapes between the metal precursor-CTAB complex and their corresponding end products, we conclude that the metal precursor-CTAB complexes shown in Figure 9 served as soft templates to shape the self-assembly structures of NCs. In other words, these metal-including micellar templates were actually present prior to the NC formation.
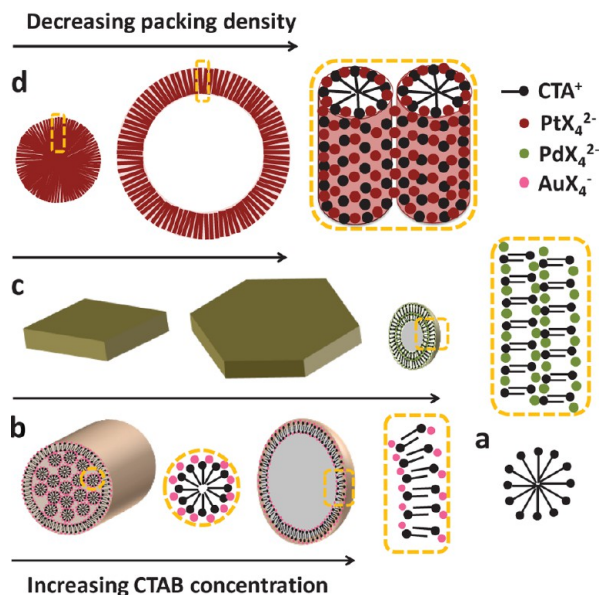
The above soft templates clearly associate with the interaction of CTAB micelles with the metal precursors. Investigations on micelle formations and micelle interaction are extensive, and they are of both theoretical[33,54−56] and practical interests.[37,57,58] Critical micelle concentration (CMC) of CTAB is at around 0.9 mM, which is also about the concentration of CTAB used in our solution A. Typical CTAB micelles are spherical in shape, their hydrodynamic radius is 2.5 nm, and they are balanced by electrostatic and steric repulsive forces from hydrophilic head interactions and hydrophobic attractive force from hydrocarbon tail interactions, as depicted in Scheme 2a. Giant micelles such as threadlike worms and large vesicles with a size above several hundred of nanometers might form due to aggregation of micelles.[59,60] The packing parameter P, $P = v/al$, where the tail length is l, the headgroup area a, and the volume of the molecule v, is used to predict shapes of a micelle.[30] In general, cases of $P < 1/3$ give spherical micelles, $1/3 < P < 1/2$ cylindrical and ellipsoidal ones, and $P > 1/2$ bilayers or formation of vesicles.[30] Although the noble metal ions are at their oxidative states, their halide complexes, namely AuCl$_4^-$, PtCl$_4^{2-}$, and PdCl$_4^{2-}$, are negatively charged, and they are counterions of CTA$^+$.

In principle, when the metal precursors are added into CTAB solution, two processes could occur spontaneously: (i) exchange of Br$^-$ (from CTAB) with Cl$^-$ in the above metal chloride complexes, which gives rise to MX$_4^{n-}$ (where M = Au^{3+}, Pt^{2+} or Pd^{2+}, X = Br$^-$ or Cl$^-$, n = 1 or 2) since Br$^-$ has a higher binding affinity toward the metal ions than Cl, and (ii) exchange of MX$_4^{n-}$ with Br$^-$ as counterions of CTA$^+$ because the metal halide complexes have a higher binding affinity than halide anions toward the headgroup of this surfactant.[61] Changes of counterions could affect the CMC, morphology, size, and reactivity of the micelles significantly.[60] Binding of MX$_4^{n-}$ to CTA$^+$ head groups screens Coulombic repulsive force among the positive head groups more efficiently than that of Br$^-$ does. As a result, the headgroup area a decreases and the packing parameter P increases accordingly. With the above two processes, small micelles could restructure themselves into giant micelles, and cylinders, bilayers, vesicles, threadlike worms at

Scheme 2. Soft Template Structures Obtained in This Work[a]

[a](a) Primary micelle of CTAB, (b) rod-shaped vesicle and spherical vesicle formed from $AuX_4^- - CTA^+$ complex, (c) various platelet assemblages formed from $PdX_4^{2-} - CTA^+$ complex with increasing CTAB concentration, and (d) dandelion-like assemblage and hollow vesicle formed from $PtX_4^{2-} - CTA^+$ complex with increasing CTAB concentration. Illustrations framed with yellow dashed lines are enlarged parts of their corresponding structures in the left. Also refer to Figures 1−7.

different spatial dimensions are common morphologies after such evolutions. Therefore, binding of MX_4^{n-} to CTA^+ head groups provides the driving force at a molecular level for the formation of giant geometric structures observed at a mesoscale level. On this basis, we could explain why the solution became turbid when the metal precursors were added to CTAB micelle solution (Figure 9a). To verify this, we have also tested the effect of reversed addition order of reactants: CTAB was first mixed with Tu alkaline solution, and then $HAuCl_4$ was added into the mixture. Not surprisingly, quasi-spherical aggregates of Au NCs with average diameter around 30 nm were produced (Figure S10), instead of rod-shaped structures (Figure 9b). This experiment confirms the important role of $MX_4^{n-} - CTA^+$ complexes as templates to guide the formation of different NC assemblages.

Nevertheless, how the micelles interact with each other and reconstruct into a hierarchical structure under certain driving force has long been a challenging issue.[37,50,33] Herein we propose that the negatively charged metal halide complex (MX_4^{n-}) serves as "electronic adhesive", connecting both the positively charged CTA^+ at a molecular scale and the micelles at a mesoscopic scale. The 1D assemblage of Au NCs is relatively simple (Figure 1). Based on Figure 9a, we believe that the giant micelle in the case of Au is interfaced with a $CTA^+ - AuX_4^-$ bilayer (Scheme 2b), together with small spherical micelles of the $CTA^+ - AuX_4^-$ complex inside this rod-shaped micelle. Different from a simple CTAB micelle (Scheme 2a), the $AuX_4^- - CTA^+$ complex in Scheme 2b is stabilized mainly by the overall balance of three types of forces: (i) hydrophobic attractive force between hydrocarbon chains, (ii) Coulombic repulsive force among the same kind of ions, and (iii) Coulombic attractive force between CTA^+ and MX_4^{n-}.

Particularly, the exposure of the hydrocarbon chains to water is thermodynamically forbidden. Therefore, a bilayer structure with its hydrophobic chains tangling with each other inside the layers and hydrophilic head facing the water could be expected (Scheme 2b). In order to maintain overall charge balance, it is expected that CTA^+ and AuX_4^- in the assemblages would distribute in an alternative fashion (Scheme 2b), or charge delocalization, resulting in "polymeric" assemblage of $-[CA-CACACA]-$, where C denotes the cation CTA^+ and A the anion AuX_4^-. In the synthesis with a high CTAB concentration, simple spherical vesicles with a $CTA^+ - AuX_4^-$ bilayer would be expected (Scheme 2b), based on the product morphology of Figure 1a.

The structures in the cases of Pt and Pd have a higher level of hierarchy. As previously discussed, cylindrical inter-particulate spaces were observed in the walls of the vesicles (Figure 3d) and in the large dandelion-shaped spheres (Figure 4f) in the case of Pt. In the case of Pd, the rhombic or hexagonal platelets were formed from coalescence of small vesicles. Therefore, two or three levels of hierarchy can be identified. The first level is the formation of "cylindrical micelles" in the case of Pt or small vesicles in the case of Pd, from the primary building blocks, i.e., the $MX_4^{n-} - CTA^+$ complex. The cylindrical structure of $PtX_4^{2-} - CTA^+$ is described in Scheme 2d, with hydrocarbon chains of CTA^+ toward the axis of micelle. In the Pd case, we assume the small vesicles could have one or more than one bilayer of $PdX_4^{2-} - CTA^+$, as suggested in Scheme 2c. Identical to the case of Au, anions of PtX_4^{2-} or PdX_4^{2-} may shield the electronic repulsive force among the CTA^+ and serve as the "electronic adhesive" to organize such supramolecular assemblies.

The above cylindrical micelles or small vesicles serve as the secondary building blocks to attain the mesoscopic assemblages through controlling micelle−micelle interaction. Note that the PtX_4^{2-} and PdX_4^{2-} anions could neutralize the surface charges of cylindrical micelles or small vesicles and reduce electrostatic repulsive force among the micelles. Also, as shown in Scheme 2d, the bivalent anions could serve as a bridge connecting any neighboring cylindrical micelles through Coulombic attractive force. In addition, van der Waals attraction force among these secondary building blocks also contributes to organization of cylindrical micelles or coalescence of small vesicles. Besides, increasing binding strength with increasing counterion valence is widely observed for the self-assembly of amphiphiles; it is also supported by the Debye−Hückle equation that ions with a higher valency are more effective in screening charges, and therefore they are better promoters for self-assembly and gel formation.[62] Consistently, as AuX_4^- is a monovalent anion whereas PtX_4^{2-} and PdX_4^{2-} are bivalent ones, the latter two could screen the repulsive electrostatic force more efficiently and serve as a tighter "electronic adhesive" to connect the micelles. This could explain why the assemblages in the latter two cases generally have higher NC number density than those in the Au case.

3.6. Role of Tu in *On-Site* Formation of NCs on Micelles. When we replaced CTAB with 100 μL of 1 wt% PVP solution and kept other conditions unchanged, small NCs were also formed (Figure S11). Nonetheless, when Tu was replaced with other reducing agents such as N_2H_4, only NPs as large as 30 nm were formed, and there was no organization among the NPs (Figure S12). The two comparative studies all point to the unique role of Tu in the formation of NCs. Tu has been widely used in industry;[63−66] the C=S bond in Tu could be oxidized

by a wide variety of oxidants.[67,68] However, to the best of our knowledge, Tu has been rarely used as a reducing agent for synthesis of noble metal NPs. Interaction of metal precursors with Tu could form either metallic NCs or metal sulfides, depending on the thermodynamic competition between redox reaction and sulfidation reaction. In particular, metallic NCs of Au and Pt are obtained as their standard oxidizing potentials are much higher (1.520 V for Au(III)/Au(0) and 1.188 V for Pt(II)/Pt(0)), but PdS NCs are formed because of a relatively low standard oxidizing potential of Pd(II)/Pd(0) (0.915 V). It has been repeatedly reported that sulfide anions could arrest the growth of gold nanorods by adsorbing on their surface as a stabilizing agent,[41] and the presence of sulfide anions promotes reduction of gold ions whereas impeding the crystal growth.[69] Our XPS analysis and elemental mapping (Figures S13 and S14) further revealed the homogeneous existence of S species in the as-formed assemblages in addition to the cationic surfactants. Therefore, it is highly plausible that the successful formation and stabilization of the small NCs are due to protection of sulfur and surfactant capping. In a control experiment (Figure S15), Tu was replaced with an equivalent dosage of Na$_2$S, and assemblages of respective NCs were also obtained, which again supported the capping role of S^{2-}. However, the resultant NCs using Na$_2$S are larger, indicating that Tu can serve better as a reducing/capping agent for synthesis of small NCs.

To understand the interaction among the reactants, intermediates formed upon mixing of solutions A and B were separated immediately. In Figure 10, such intermediates bear
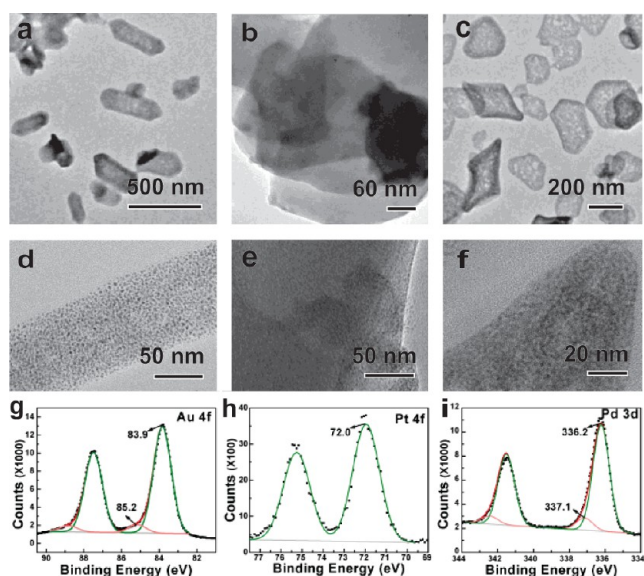

Figure 10. TEM images of intermediates (i.e., assemblages of metal sulfide NCs) formed immediately (within 1 min) upon mixing solution A and solution B for the cases of (a,d) Au, (b,e) Pt, and (c,f) Pd. r_c is 1:1; and XPS spectra of (g) Au 4f, (h) Pt 4f, and (i) Pd 3d of the intermediates.

very similar structural features to their final NC assemblages. Furthermore, intermediates obtained in the cases of Au and Pd are as stable as their final NC assemblages under an electron beam.

When the solution of HAuCl$_4$ and CTAB (i.e., solution B) was added into alkaline Tu (i.e., solution A), the reaction system became yellowish brown instantly, which is a typical

color of colloidal Au$_2$S (Figure S16).[69] The XPS analysis of this intermediate is reported in Figure 10g. A major BE peak of Au 4f$_{7/2}$ is observed at 83.9 eV, which is around 0.3 eV higher than that of Au(0) species detected in the end product. The bond of Au$_2$S has mixed ionic and covalent properties, and BE of Au species in Au$_2$S is at 83.9 or 84.0 eV for Au 4f$_{7/2}$, which is almost the same as Au(0) species.[69−71] Our UV−vis spectrum of the mixture of A and B solutions (Figure S16) is identical to that of Au$_2$S NPs.[69−71] The intensity over 300−500 nm decreased monotonically (Figure S16), and the yellowish brown color faded away gradually with increasing reaction time. Finally, the color of mixture became lightly opalescent, and the UV−vis spectrum of the product has a much lower intensity within the UV range (Figure S16). The color change, XPS analysis, and UV−vis spectral evolution altogether confirmed the instant generation of Au$_2$S upon mixing AuX$_4^-$−CTAB with alkaline Tu. The XPS spectra of Pt(II) in PtS and Pd(II) in PdS also have similar characteristics as that of Au$_2$S. As shown in Figure 10h, the BE of Pt 4f$_{7/2}$ is 72.0 eV, which is 0.8 eV higher than that of the metallic Pt(0) in the end product, confirming the formation of PtS intermediate. In Figure 10i, however, the BE of Pd 3d is the same as that of the end product, that is, Pd(II) in PdS NCs, as we have discussed in Figure 6f.

It has also been confirmed that there is no free gold ions in the presence of CTAB.[41,72] The reduction of Au(III) to Au(I) (which is a very fast reaction) and precipitation reaction between Au(I) and S^{2-} would occur at the interface of micelle and water in an *on-site* manner. In principle, for any crystallization process, the ratio (R) of growth rate (R_G) to nucleation rate (R_N), $R = R_G/R_N$, determines the size of NCs.[73,74] Smaller values of R, i.e., fast nucleation kinetics and slow crystal growth, correlate to smaller NCs and *vice versa*. A fast nucleation rate requires a high degree of supersaturation of matrix solution.[75] Heavy metal sulfides, due to their small K_{sp}, could easily achieve a strong supersaturation state and precipitate even at very low concentrations of solutes.[76] In our present work, Tu in solution A would undergo hydrolysis to release S^{2-} under alkaline condition according to eq 1.[77]

$$SC(NH_2)_2 + 2OH^- \leftrightarrow S^{2-} + H_2CN_2 + 2H_2O \qquad (1)$$
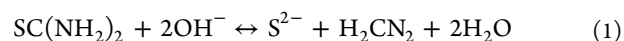
Mixing solution A with solution B would lead to fast nucleation, as described in reaction 2, where MS$_{(NC)}$ or M$_2$S$_{(NC)}$ denotes

$$MX_4^{n-} + S^{2-} \rightarrow MS_{(NC)} \text{ or } M_2S_{(NC)} \qquad (2)$$

the resultant metal sulfide NCs. It is known that the hydrolysis of Tu is reversible (reaction 1, $K = 2.25 \times 10^{-15}$) and the hydrolysis rate decreases with decreasing pH value.[77] Since solution B is acidic, Tu would experience a pH fall upon mixing solution A with solution B, and the hydrolysis rate would decrease. Different from those in simple dissociation of Na$_2$S, the S^{2-} ions from Tu hydrolysis are released in a controllable way, and the temporal S^{2-} concentration is relatively low when solution A is mixed with solution B, resulting in a slow growth rate for the as-formed nuclei of metal sulfides. Clearly, such a scenario would be associated with a small R value and thus formation of small NCs.

Two factors can be attributed to the conservation of the pristine shapes of CTA$^+$−MX$_4^{n-}$ templates after the above reactions. The first one lies in the charge-neutral property of

Tu, due to which the addition of Tu exerts the least morphological impact on the inorganic–organic templates. On the contrary, product structures synthesized with Na_2S deviate away the $CTA^+-MX_4^{n-}$ template noticeably (Figure S15) because of sudden increase in S^{2-} anions. Localized generation of NCs is another important factor for stabilizing final product. In reaction 2, CTA^+ ions could be liberated from $CTA^+-MX_4^{n-}$ pairs when the MX_4^{n-} was converted to NCs. Such NCs possess highly active solid–liquid interface (with high Gibbs energy) which can accommodate the released CTA^+ molecules without causing drastic structural disruption. Meanwhile, the hydrophobic tails of CTA^+ remained engaged with each other (Figure 2e, Figure 5e, and Figure 7e), maintaining overall structural integrity.

The formation of NCs of metal sulfides (Figure 10) is also critical to ensure the small size of the final metal NCs. In the first place, for example, the Au_2S NCs could serve as seeds to provide active sites for sulfide to metal conversion. Second, compared with free Au(I) ions or Au(I) chloride complex, for example, Au_2S is more stable,[69] serving as a temporary reservoir of both reductant (i.e., S^{2-}) and oxidant (i.e., Au(I)). After the nucleation, concentrations of free reductants (Tu and S^{2-}) and free oxidant (Au(I)) are very low, and the conversion of Au_2S to Au NCs (i.e., eq 3) becomes predominant.

$$MS_{(NC)} \text{ or } M_2S_{(NC)} \rightarrow M_{(NC)} \tag{3}$$
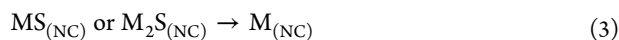
3.7. Preliminary Study on Catalytic Performance of NCs.
The present giant micelle-assisted synthesis and self-assembly of Au, Pt, and Pd NCs provide an easy approach to preparation of noble metal-based nanocatalysts. Nevertheless, it should be mentioned that TGA analysis revealed (Figure S17) that in the original PdS platelets, total organics such as sulfur-containing species and surfactant molecules account for ca. 52% of the total weight. The large amount of capping agents is necessary to form the NC assemblages, but they might passivate active sites of the NCs. Herein, to test the catalytic activity of these NCs, the Pd rhombic/hexagonal platelets were used for the reduction of 4-NP to 4-aminophenol (4-AP) by $NaBH_4$. The reaction was conducted with molar ratio of 4-NP to $NaBH_4$ to Pd as 1:176.1:0.12. PdS NCs was converted to Pd NCs instantly when the catalyst of colloidal PdS NC assemblages was added into the deep yellow mixture of 4-NP and $NaBH_4$. Within 10 min, the deep yellow color was gone. After removing the catalyst Pd NCs, the solution was transparent and clear. Figure 11a shows the spectroscopic evolution of the reaction solution. As can be seen, the band of 4-NP centered at 400 nm decreased rapidly with the reaction time, whereas a small band at 300 nm emerged, corresponding to the transformation of 4-NP into 4-AP. The absorbance (A) of the solution at 400 nm was plotted against the reaction time (t); the data set could be fitted to $A = A_0 e^{-kt}$ according to the first-order reaction rate law (Figure S18),[78] and the rate constant (k) obtained is 6.0×10^{-3} s^{-1} at 23 °C. The NCs exist in the form of assemblages, which renders the catalysts with advantage similar to the conventional supported catalysts, facilitating their separation after use.

The catalytic stability of the assemblages was also studied. In Figure 11b, there is no sign of losing catalytic activity after eight repeated cycles of reaction. TEM images of a spent catalyst are shown in Figure 11c,d. The mesoscopic platelet structure is well maintained after all these reactions. Nonetheless, due to the
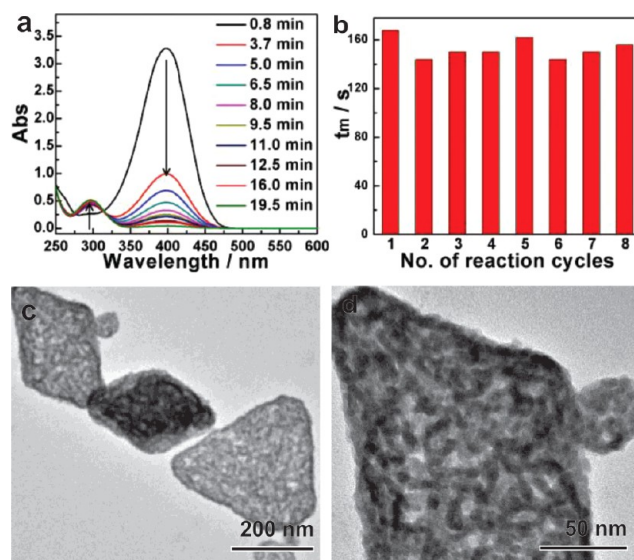
Figure 11. (a) UV–vis spectra of the reaction solution (after removal of catalyst) in the reduction of 4-nitrophenol to 4-aminophenol catalyzed by Pd NC assemblages. (b) Catalytic stability of the Pd NCs, where t_m is the minimum reaction time required to complete the reduction (with the same amounts of 4-NP and $NaBH_4$ in each run). [Note: The concentration of $NaBH_4$ in these experiments was much higher than that used in (a); see Experimental Section.] (c,d) TEM images at different magnifications for the spent Pd catalyst after eight reaction cycles.

hash working environment, oriented attachment occurred among neighboring Pd NCs, giving rise to a porous metallic framework formed by inter-connected nanowires with diameters at ca. 5 nm (Figure 11d and Figure S19). Such Pd metallic platelets could be considered as a freestanding nanocatalyst which has higher stability than their softer counterpart PdS NC assemblages. What is more, our TGA analysis revealed that the total organics within the metallic platelets accounts for 11.5%, which is much lower than that in the PdS NC assemblages (versus the organic content 52%, Figure S17). Clearly, different NC assemblages have different extents of stability depending on their compactness and reaction conditions. For example, the Au NC assemblages are very loose, and they undergo aggregation (30 nm in size) in acidic pH condition. Such changeable NC assemblages can also be viewed as designed catalyst precursors for us to develop freestanding metallic nanocatalysts with structural and compositional controls.

4. CONCLUSIONS
In summary, mesoscale hierarchical assemblages of aqueous soluble Au, Pt, and Pd NCs were generated with well-defined boundaries using their respective halide salts, Tu as a reductant, and CTAB as a surfactant. The geometric shape, structural hierarchy complexity, and packing density of the assembled products vary depending on the nature of metal precursors and the CTAB concentration. For the Au case, one-dimensional "nanorod" assemblages were formed, and they could restructure into hollow vesicles with additional CTAB. For the Pt case, giant vesicles were first formed, and they could then evolve into dandelion-like spherical assemblages through the budding process at a lower CTAB concentration. And for the Pd case, rhombic/hexagonal structures were resulted from coalescence of small vesicles. Giant micelles of CTAB–metal halide complexes with similar geometric shapes to the final metal

NC assemblages were found to serve as soft-templates to direct synthesis and assembly of NCs. Molecularly, the metal halide complex anions (MX_4^{n-}, M = Au, Pt, and Pd) could bind to CTA^+ cations with a higher affinity than Br^- and efficiently screen the electrostatic repulsive force among the positively charged CTA^+, which provides the driving force for the formation of hierarchical giant micelles. At a mesoscopic level, the metal halide anions work as an "electronic adhesive" which can either neutralize neighboring CTA^+ cations within a micelle or connect adjacent micelles to form a larger one. The successful formation of metal NCs could be explained from the perspective of crystallization kinetics. The unique protection of sulfide species and the controlled release of S^{2-} from Tu were important to suppress rapid growth of metal sulfide intermediates, thus ensuring the size control for final metal NCs (≤ 3 nm). Furthermore, our preliminary catalytic study also demonstrated that the assemblages of metal NCs have high activity and reusability.

The importance of the above results lies in the following three aspects: (i) Structural features originated from the self-assembly of the CTA−metal halide micelles are well succeeded by the metal NC assemblages, elucidating a micelle-assisted approach for self-assembly of NCs or NPs into hierarchical structures. (ii) Stabilized geometric shapes of NC assemblages (i.e., with the silica capping shell) directly record the self-assembly behaviors of metal precursors and hydrocarbon surfactants as well as micellar interaction and chemical transformation. This method thus provides a convenient means for visualization of dynamical colloidal processes, complementary to state-of-the-art analytical techniques such as cryo-TEM, small-angle X-ray scattering, etc. (iii) Mesoscale organization of Au, Pt, and Pd NCs offers an alternative to prepare water-soluble porous noble metal catalysts. Such self-assembled nanocatalysts with a high load (above 50%) of active component can perform effectively in terms of metal utilization, mass transport, and product separation.

■ ASSOCIATED CONTENT

Ⓢ Supporting Information
Data from LLS analysis, TEM images of samples studied at other experimental conditions, XPS spectra of S species and EDX analysis of some representative samples, UV−vis spectra, TGA analysis, and kinetic data of 4-NP reduction reaction. This material is available free of charge via the Internet at http://pubs.acs.org.

■ AUTHOR INFORMATION

Corresponding Author
chezhc@nus.edu.sg
Notes
The authors declare no competing financial interest.

■ ACKNOWLEDGMENTS

■ REFERENCES

(1) Jana, N. R.; Peng, X. *J. Am. Chem. Soc.* **2003**, *125*, 14280.

(2) Chauhan, B. P.; Rathore, J. S. *J. Am. Chem. Soc.* **2005**, *127*, 5790.

(3) Hara, T.; Mori, K.; Oshiba, M.; Mizugaki, T.; Ebitani, K.; Kaneda, K. *Green Chem.* **2004**, *6*, 507.

(4) Xu, W.; Ni, J.; Zhang, Q.; Feng, F.; Xiang, Y.; Li, X. *J. Mater. Chem. A* **2013**, *1*, 12811.

(5) Jain, P. K.; Huang, X.; El-Sayed, I. H.; El-Sayed, M. A. *Acc. Chem. Res.* **2008**, *41*, 1578.

(6) Tsunoyama, H.; Sakurai, H.; Negishi, Y.; Tsukuda, T. *J. Am. Chem. Soc.* **2005**, *127*, 9374.

(7) Zhu, M.; Aikens, C. M.; Hollander, F. J.; Schatz, G. C.; Jin, R. *J. Am. Chem. Soc.* **2008**, *130*, 5883.

(8) Wang, Y.; Ren, J.; Deng, K.; Gui, L.; Tang, Y. *Chem. Mater.* **2000**, *12*, 1622.

(9) Le Guével, X.; Trouillet, V.; Spies, C.; Jung, G.; Schneider, M. *J. Phys. Chem. C* **2012**, *116*, 6047.

(10) Zhou, C.; Sun, C.; Yu, M.; Qin, Y.; Wang, J.; Kim, M.; Zheng, J. *J. Phys. Chem. C* **2010**, *114*, 7727.

(11) Brust, M.; Walker, M.; Bethell, D.; Schiffrin, D. J.; Whyman, R. *J. Chem. Soc., Chem. Commun.* **1994**, 801.

(12) Lee, D.; Donkers, R. L.; Wang, G.; Harper, A. S.; Murray, R. W. *J. Am. Chem. Soc.* **2004**, *126*, 6193.

(13) Yang, J.; Lee, J. Y.; Deivaraj, T.; Too, H.-P. *Langmuir* **2003**, *19*, 10361.

(14) Zhu, M.; Qian, H.; Jin, R. *J. Am. Chem. Soc.* **2009**, *131*, 7220.

(15) Crooks, R. M.; Zhao, M.; Sun, L.; Chechik, V.; Yeung, L. K. *Acc. Chem. Res.* **2001**, *34*, 181.

(16) Scott, R. W.; Wilson, O. M.; Crooks, R. M. *J. Phys. Chem. B* **2005**, *109*, 692.

(17) Yang, X.; Shi, M.; Zhou, R.; Chen, X.; Chen, H. *Nanoscale* **2011**, *3*, 2596.

(18) Israelachvili, J. N.; Mitchell, D. J.; Ninham, B. W. *J. Chem. Soc., Faraday Trans. 2* **1976**, *72*, 1525.

(19) Pileni, M.-P. *Nat. Mater.* **2003**, *2*, 145.

(20) Liu, J.; Qiao, S. Z.; Budi Hartono, S.; Lu, G. Q. M. *Angew. Chem.* **2010**, *122*, 5101.

(21) Nikolic, M. S.; Olsson, C.; Salcher, A.; Kornowski, A.; Rank, A.; Schubert, R.; Frömsdorf, A.; Weller, H.; Förster, S. *Angew. Chem., Int. Ed.* **2009**, *48*, 2752.

(22) He, J.; Wei, Z.; Wang, L.; Tomova, Z.; Babu, T.; Wang, C.; Han, X.; Fourkas, J. T.; Nie, Z. *Angew. Chem.* **2013**, *125*, 2523.

(23) Song, J.; Cheng, L.; Liu, A.; Yin, J.; Kuang, M.; Duan, H. *J. Am. Chem. Soc.* **2011**, *133*, 10760.

(24) Mai, Y.; Eisenberg, A. *J. Am. Chem. Soc.* **2010**, *132*, 10078.

(25) Toyota, T.; Ohguri, N.; Maruyama, K.; Fujinami, M.; Saga, T.; Aoki, I. *Anal. Chem.* **2012**, *84*, 3952.

(26) Wang, D. P.; Zeng, H. C. *Chem. Mater.* **2011**, *23*, 4886.

(27) Kao, J.; Thorkelsson, K.; Bai, P.; Rancatore, B. J.; Xu, T. *Chem. Soc. Rev.* **2013**, *42*, 2654.

(28) Schnur, J. M. *Science* **1993**, *262*, 1669.

(29) Fenyves, R.; Schmutz, M.; Horner, I. J.; Bright, F. V.; Rzayev, J. *J. Am. Chem. Soc.* **2014**, *136*, 7762.

(30) Goyal, P.; Aswal, V. *Curr. Sci.—Bangalore* **2001**, *80*, 972.

(31) Qiu, H.; Cambridge, G.; Winnik, M. A.; Manners, I. *J. Am. Chem. Soc.* **2013**, *135*, 12180.

(32) Almgren, M. *Aust. J. Chem.* **2003**, *56*, 959.

(33) Vauthey, S.; Santoso, S.; Gong, H.; Watson, N.; Zhang, S. *Proc. Natl. Acad. Sci. U.S.A.* **2002**, *99*, 5355.

(34) Davies, T. S.; Ketner, A. M.; Raghavan, S. R. *J. Am. Chem. Soc.* **2006**, *128*, 6669.

(35) Xiong, Y.; Xie, Y.; Yang, J.; Zhang, R.; Wu, C.; Du, G. *J. Mater. Chem.* **2002**, *12*, 3712.

(36) Warren, S. C.; Messina, L. C.; Slaughter, L. S.; Kamperman, M.; Zhou, Q.; Gruner, S. M.; DiSalvo, F. J.; Wiesner, U. *Science* **2008**, *320*, 1748.

(37) Ruthstein, S.; Schmidt, J.; Kesselman, E.; Popovitz-Biro, R.; Omer, L.; Frydman, V.; Talmon, Y.; Goldfarb, D. *Chem. Mater.* **2008**, *20*, 2779.

(38) Stein, A.; Melde, B. J.; Schroden, R. C. *Adv. Mater.* **2000**, *12*, 1403.

13816

dx.doi.org/10.1021/ja506905j | *J. Am. Chem. Soc.* 2014, 136, 13805−13817

(39) Attard, G. S.; Corker, J. M.; Göltner, C. G.; Henke, S.; Templer, R. H. *Angew. Chem., Int. Ed.* **1997**, *36*, 1315.

(40) Yamauchi, Y.; Sugiyama, A.; Morimoto, R.; Takai, A.; Kuroda, K. *Angew. Chem., Int. Ed.* **2008**, *47*, 5371.

(41) Zweifel, D. A.; Wei, A. *Chem. Mater.* **2005**, *17*, 4256.

(42) Zhang, Y. X.; Zeng, H. C. *J. Phys. Chem. C* **2007**, *111*, 6970.

(43) Zheng, J.; Petty, J. T.; Dickson, R. M. *J. Am. Chem. Soc.* **2003**, *125*, 7780.

(44) Sen, F.; Gökagaç, G. *J. Phys. Chem C* **2007**, *111*, 5715.

(45) Lipowsky, R. *J. Biol. Phys.* **2002**, *28*, 195.

(46) Jülicher, F.; Lipowsky, R. *Phys. Rev. E* **1996**, *53*, 2670.

(47) Jülicher, F.; Lipowsky, R. *Phys. Rev. Lett.* **1993**, *70*, 2964.

(48) Ng, Y. H.; Wang, M.; Han, H.; Chai, C. L. *Chem. Commun.* **2009**, 5530.

(49) Vinkevičius, J.; Jankauskas, E.; Čerškienė, I.; Jasulaitienė, V.; Vaškelis, A. *Chemija* **2004**, *15*, 11.

(50) Gustafsson, J.; Ljusberg-Wahren, H.; Almgren, M.; Larsson, K. *Langmuir* **1997**, *13*, 6964.

(51) Li, Z.; Hillmyer, M. A.; Lodge, T. P. *Nano Lett.* **2006**, *6*, 1245.

(52) Ross, S. *Ind. Eng. Chem. Res.* **1969**, *61*, 48.

(53) Stamenović, D. *J. Colloid Interface Sci.* **1991**, *145*, 255.

(54) Lima, F. S.; Cuccovia, I. M.; Horinek, D.; Amaral, L. Q.; Riske, K. A.; Schreier, S.; Salinas, R. K.; Bastos, E. L.; Pires, P. A.; Bozelli, J. C., Jr. *Langmuir* **2013**, *29*, 4193.

(55) Rodrigues, R. K.; Ito, T. H.; Sabadini, E. *J. Colloid Interface Sci.* **2011**, *364*, 407.

(56) Subramanian, V.; Ducker, W. A. *Langmuir* **2000**, *16*, 4447.

(57) Ruthstein, S.; Schmidt, J.; Kesselman, E.; Talmon, Y.; Goldfarb, D. *J. Am. Chem. Soc.* **2006**, *128*, 3366.

(58) Omer, L.; Ruthstein, S.; Goldfarb, D.; Talmon, Y. *J. Am. Chem. Soc.* **2009**, *131*, 12466.

(59) Lin, Z.; Cai, J.; Scriven, L.; Davis, H. *J. Phys. Chem.* **1994**, *98*, 5984.

(60) Feitosa, E.; Savério Brazolin, M. R.; Zumstein Georgetto Naal, R. M.; Perpétua Freire de Morais Del Lama, M.; Lopes, J. R.; Loh, W.; Vasilescu, M. *J. Colloid Interface Sci.* **2006**, *299*, 883.

(61) Pérez-Juste, J.; Liz-Marzan, L.; Carnie, S.; Chan, D. Y.; Mulvaney, P. *Adv. Funct. Mater.* **2004**, *14*, 571.

(62) Stendahl, J. C.; Rao, M. S.; Guler, M. O.; Stupp, S. I. *Adv. Funct. Mater.* **2006**, *16*, 499.

(63) Li, H.; Wang, J.; Li, H.; Yin, S.; Sato, T. *Res. Chem. Intermed.* **2010**, *36*, 27.

(64) Jayalakshmi, M.; Rao, M. M. *J. Power Sources* **2006**, *157*, 624.

(65) Rao, M. M.; Jayalakshmi, M.; Reddy, R. S. *Chem. Lett.* **2004**, *33*, 1044.

(66) Li, J.; Miller, J. *Hydrometallurgy* **2002**, *63*, 215.

(67) Shubha, J.; Puttaswamy. *J. Sulfur Chem.* **2009**, *30*, 490.

(68) Zhu, T. *Hydrometallurgy* **1992**, *28*, 381.

(69) Mikhlin, Y.; Likhatski, M.; Karacharov, A.; Zaikovski, V.; Krylov, A. *Phys. Chem. Chem. Phys.* **2009**, *11*, 5445.

(70) Kuo, C.-L.; Huang, M. H. *J. Phys. Chem. C* **2008**, *112*, 11661.

(71) Morris, T.; Copeland, H.; Szulczewski, G. *Langmuir* **2002**, *18*, 535.

(72) Torigoe, K.; Esumi, K. *Langmuir* **1992**, *8*, 59.

(73) Watzky, M. A.; Finke, R. G. *Chem. Mater.* **1997**, *9*, 3083.

(74) Zhou, Y.; Wang, H.; Lin, W.; Lin, L.; Gao, Y.; Yang, F.; Du, M.; Fang, W.; Huang, J.; Sun, D. *J. Colloid Interface Sci.* **2013**, *407*, 8.

(75) Mersmann, A. *Chem. Eng. Process.* **1999**, *38*, 345.

(76) Cervantes, F. J.; Pavlosthathis, S. G.; Van Haandel, A. C. *Advanced biological treatment processes for industrial wastewaters: principles and applications*; IWA Publishing: London, 2006.

(77) Mokili, B.; Froment, M.; Lincot, D. *J. Phys. IV* **1995**, *5*, C3.

(78) Yang, Y.; Hao, S.; Sun, C.; Ren, Y. *Green Chem.* **2014**, *16*, 2273.

13817

dx.doi.org/10.1021/ja506905j | *J. Am. Chem. Soc.* **2014**, *136*, 13805−13817